

Article

Charge Transport Mechanism in the Forming-Free Memristor Based on PECVD Silicon Oxynitride

Andrei A. Gismatulin ^{1,*}, Gennadiy N. Kamaev ¹, Vladimir A. Volodin ^{1,2,*} and Vladimir A. Gritsenko ^{1,3}¹ Rzhanov Institute of Semiconductor Physics SB RAS, Lavrentiev Ave. 13, 630090 Novosibirsk, Russia² Physical Department, Novosibirsk State University, Pirogova Street 2, 630090 Novosibirsk, Russia³ Faculty of Automation and Computer Engineering, Novosibirsk State Technical University, 20 Prospekt K. Marksa, 630073 Novosibirsk, Russia

* Correspondence: aagismatulin@isp.nsc.ru (A.A.G.); volodin@isp.nsc.ru (V.A.V.)

Abstract: A memristor is a new generation memory that merges dynamic random access memory and flash properties. In addition, it can be used in neuromorphic electronics. The advantage of silicon oxynitride, as an active memristor layer, over other dielectrics is its compatibility with silicon technology. It is expected that SiN_xO_y-based memristors will combine the advantages of memristors based on nonstoichiometric silicon oxides and silicon nitrides. In the present work, the plasma-enhanced chemical vapor deposition (PECVD) method was used to fabricate a silicon oxynitride-based memristor. The memristor leakage currents determine its power consumption. To minimize the power consumption, it is required to study the charge transport mechanism in the memristor in the high-resistance state and low-resistance state. The charge transport mechanism in the PECVD silicon oxynitride-based memristor in high and low resistance states cannot be described by the Schottky effect, thermally assisted tunneling model, Frenkel effect model of Coulomb isolated trap ionization, Hill–Adachi model of overlapping Coulomb potentials, Makram–Ebeid and Lannoo model of multiphonon isolated trap ionization, Nasyrov–Gritsenko model of phonon-assisted tunneling between traps, or the Shklovskii–Efros percolation model. The charge transport in the forming-free PECVD SiO_{0.9}N_{0.6}-based memristor in high and low resistance states is described by the space charge limited current model. The trap parameters responsible for the charge transport in various memristor states are determined. For the high-resistance state, the trap ionization energy W is 0.35 eV, and the trap concentration N_d is $1.7 \times 10^{19} \text{ cm}^{-3}$; for the low-resistance state, the trap ionization energy W is 0.01 eV, and the trap concentration N_t is $4.6 \times 10^{17} \text{ cm}^{-3}$.

Keywords: silicon oxynitride; memristors; charge transport

Citation: Gismatulin, A.A.; Kamaev, G.N.; Volodin, V.A.; Gritsenko, V.A. Charge Transport Mechanism in the Forming-Free Memristor Based on PECVD Silicon Oxynitride.

Electronics **2023**, *12*, 598. <https://doi.org/10.3390/electronics12030598>

Academic Editor: Costas Psychalinos

Received: 29 December 2022

Revised: 23 January 2023

Accepted: 23 January 2023

Published: 25 January 2023



Copyright: © 2023 by the authors. Licensee MDPI, Basel, Switzerland. This article is an open access article distributed under the terms and conditions of the Creative Commons Attribution (CC BY) license (<https://creativecommons.org/licenses/by/4.0/>).

1. Introduction

Silicon oxynitride (SiN_xO_y) is a promising material, and it has very wide applications in different fields [1]. However, we will focus only on one of the silicon oxynitride applications as a memristor element [2]. A memristor is an element that can switch between high resistance state (HRS) and low resistance state (LRS) and save those states for 10 years at 85 °C [3,4]. SiN_xO_y is the mixture between silicon oxide (SiO₂) and silicon nitride (Si₃N₄) [5,6]. SiO₂ and Si₃N₄ are still the main materials used in silicon technology. Hence, the undoubted advantage of SiN_xO_y is that it is compatibility with standard technological processes of modern silicon microelectronics. SiN_xO_y is already used in logic devices as a thin layer (0.5–0.7 nm) at the interfaces with silicon when using high- k dielectrics to create a transistor gate. It is expected that memristors based on SiN_xO_y will combine the advantages of memristors based on nonstoichiometric silicon oxide (SiO_x) and silicon nitride (SiN_x), which are currently studied on a wide front [7–10]. According to our previous research data, the performance of SiO_x-based memristors is higher than that of SiN_x-based memristors [9,10]; the switching voltage in the SiO_x-based memristors (+10 V and –10 V)

is lower than in the SiN_x -based memristors (+10 V and -16 V) with similar leakage current in the LRS and HRS. Therefore, the power consumption in the SiO_x -based memristors is less than in the SiN_x -based memristors. On the other hand, SiN_x -based memristors are characterized by a longer storage time [9,10]. The SiN_xO_y -based memristors have a wide range of control of physical properties through the ability to vary the chemical composition, which opens up the possibility of controlling the memory properties. In addition, it can be expected that SiN_xO_y -based memristors will have a higher information storage time than SiO_x -based memristors. This hypothesis is based on the fact that the information storage time is determined by the defect diffusion involved in the conductive filament forming (filament consists of nitrogen vacancies for SiN_x -based memristors and of oxygen vacancies for SiO_x -based memristors), and the nitrogen self-diffusion coefficient value ($0.212 \text{ cm}^{-2}/\text{s}$ at 25°C [11]) is lower than that of oxygen ($0.232 \text{ cm}^{-2}/\text{s}$ [11]). The diffusion coefficient value of nitrogen in SiN_x [12] and the diffusion coefficient value of oxygen in SiO_x [13] are more difficult to compare due to their very strong diffusion coefficient dependence on temperature and the layer-forming technique [13]. Finally, SiN_xO_y -based memristors should have a higher performance than SiN_x -based memristors due to the lower nitrogen vacancy formation energy compared to the silicon vacancy.

The memristor is very sensitive to the obtaining by the active layer technology and contacts to the active area. As an example, the $\text{GeO}[\text{SiO}_2]$ -based memristor has a better memory window (LRS/HRS ratio) than the $\text{GeO}[\text{SiO}]$ -based memristor with the same contacts [14]. Silicon oxynitride films can be obtained by various methods: magnetron deposition [15], low-pressure chemical vapor deposition [16] and plasma-enhanced chemical vapor deposition (PECVD) [17]. The advantage of the PECVD method for the silicon oxynitride film is low deposition temperature that can be used to easier integrate the PECVD silicon oxynitride film in the formation of crossbar structures.

Usually, the charge transport in silicon oxynitride layers is described by the Frenkel effect [18,19]. Recently, it has been established that the model of phonon-assisted tunneling between neighboring traps describes the charge transport in the chemical vapor deposition of SiN_xO_y [20]. We studied the charge transport mechanism in detail in forming-free PECVD SiO_x [9] and forming-free PECVD SiN_x [10]. We also studied in detail the electronic structure and optical properties of different composition PECVD SiN_xO_y films for memristor applications [21]. Few papers study the charge transport mechanism in depth. In [16], SiN_xO_y film was obtained by the oxygen plasma treatment of LPCVD silicon nitride. As a result, the authors obtained the memristor with a SiN_xO_y layer and a silicon nitride layer. In this work, they explained the charge transport mechanism by the space-charge limited current (SCLC) model, but the modelling of experimental data was made only for the Si_3N_4 -based memristor in the HRS. Thus, the aim of this work is to determine the charge transport mechanism in the PECVD SiN_xO_y memristor and estimate the trap concentration and trap ionization energy.

2. Materials and Methods

$\text{SiN}_x\text{O}_y\text{:H}$ films were obtained by PECVD with a gas mixture of SiH_4 , N_2 , and O_2 on p^{++} -type Si (100) wafers after the RCA-1 cleaning procedure followed by oxide removal in diluted hydrofluoric acid, a final rinsing in deionized water, and drying in a nitrogen stream. However, after all the procedures, the loading of the substrate into the PECVD chamber was carried out through air; accordingly, the silicon was covered with a fresh natural oxide layer. The PECVD unit has a wide-aperture inductive plasma source with frequency 13.56 MHz and a turbomolecular pump. The residual pressure in the reactor was less than 10^{-6} Torr. The substrate temperature was set at 200°C and maintained during the deposition process automatically by a heater. The SiH_4 flow was constantly supplied to the reaction zone (gas mixture of 10% SiH_4 diluted with Ar) and its supply rate was 10 sccm. The films were obtained at the nitrogen flow rate value of 6 sccm. This nitrogen flow value range is optimal (as it was found earlier when studying the PECVD SiN_xO_y films). If we applied a lower nitrogen flow, the obtained samples were not suitable for

the memristor application. If we applied a higher nitrogen flow, the nitrogen content in plasma increased very slowly. Nitrogen gas was diluted with oxygen so that the oxygen concentration in the mixture was less than 1%. The low oxygen content in the gas mixture is needed to obtain the films highly enriched with silicon because oxygen has a very high chemical activity with silicon. In addition, the high oxidation rate is expected because of the presence of Ar [22]. The film was formed at the 6 sccm N₂ flow and plasma generator power 150 W. The silicon oxynitride films with a thickness of about 33 nm were obtained with this PECVD method. The film composition was studied using the method of X-ray photoelectron spectroscopy (XPS). Based on the intensity of the peaks of silicon, oxygen, and nitrogen in the XPS spectra, the composition was determined as SiO_{0.9}N_{0.6}. To obtain the metal–dielectric–semiconductor memristor structure, the nickel electrodes were deposited through a metal mask using magnetron sputtering in the Ar atmosphere. The obtained nickel electrodes had a 200 nm thickness and a 0.5 mm² area. A continuous 200 nm thick nickel layer was deposited on the p⁺⁺-type back substrate side.

The current–voltage measurements were carried out in the temperature range of 300 to 400 K in the LTS420E Linkam cell by using the Keithley 2400 and temperature controller Linkam T95 devices. The voltage ramp rate used for the current–voltage measurements was 0.9 V/s.

To clarify the charge transport mechanism, the temperature current–voltage (IV) characteristics were taken for the PECVD SiO_{0.9}N_{0.6}-based memristor in the HRS and LRS. These characteristics were compared with two contact-limited models, namely, the Schottky effect model [23] and the thermally assisted tunneling (TAT) mechanisms [24,25], and six bulk-limited models, namely, the Frenkel effect model of Coulomb isolated trap ionization [26,27], the Hill–Adachi (H-A) model of overlapping Coulomb potentials [28,29], the Makram–Ebeid and Lannoo (ME-L) model of multiphonon isolated trap ionization [30], the Nasyrov–Gritsenko (N-G) model of phonon-assisted tunneling between traps [31], the Shklovskii–Efros (S-E) percolation model [32,33], and the SCLC model [34–37].

In the Schottky effect, the current is limited by the thermal electron emission through the barrier, which is reduced due to image forces (Figure 1a) [23]. The Schottky effect current is described by the following equation:

$$I = AST^2 \exp \left(- \frac{W_0 - \left(\frac{e^3}{4\pi\epsilon_\infty\epsilon_0} \right)^{1/2} \sqrt{\frac{U}{d}}}{kT} \right), \quad (1)$$

$$A = \frac{4\pi m^* k^2 e}{m_e h^3} = 120.4 \frac{m^*}{m_e} \left[\frac{A}{\text{cm}^2 \text{K}^2} \right]$$

where I —current, A —Richardson–Deshman constant, S —contact area, T —temperature, W_0 —potential barrier height at the metal/SiO_xN_y interface, U —voltage, d —dielectric thickness, k —Boltzmann constant, e —electron charge, $\epsilon_\infty = n^2$ —high-frequency dielectric permittivity, n —refractive index, ϵ_0 —dielectric constant, m^* —electron effective mass, m_e —electron mass, h —Plank constant.

The TAT model describes the charge transport mechanism, where an electron, after the phonon absorption, is excited to a certain energy value and then tunnels through a triangle barrier (Figure 1b) [24,25]. The current for the TAT model has the following formula [24,25]:

$$I = \sqrt{2\pi m^* kT} \left(\frac{e}{h} \right)^2 S \frac{U}{d} \exp \left(- \frac{W_0 - \frac{1}{6} \left(\frac{he \times \left(\frac{U}{d} \right)}{4\pi kT \sqrt{m^*}} \right)^2}{kT} \right), \quad (2)$$

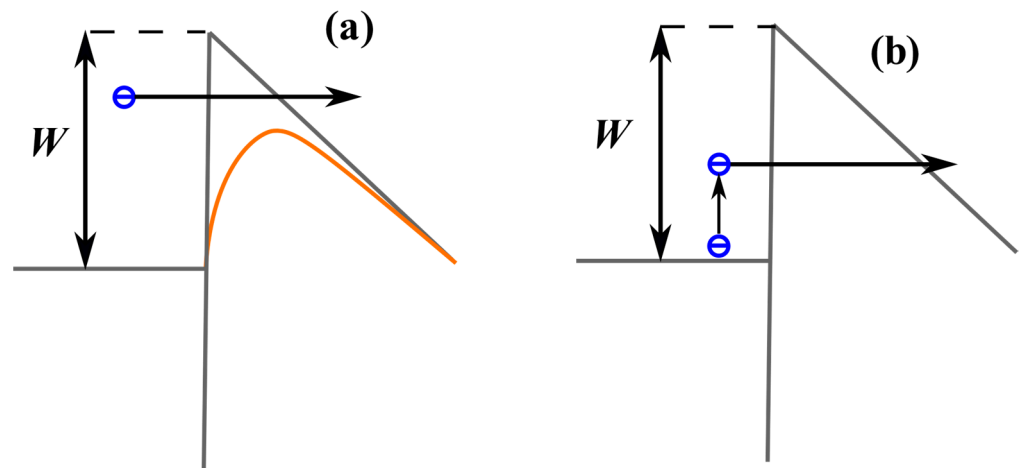


Figure 1. Schematic diagram of contact-limited models: (a) Schottky effect, (b) thermally assisted tunneling model.

The current I through the material-containing traps can be described by the following equation [20]:

$$I = eN^{2/3}SP \tag{3}$$

where $N = a^{-3}$ —trap concentration, a —average distance between traps, S —contact area, and P —trap ionization probability.

The Frenkel effect is due to a lower Coulomb positively charged trap potential in a strong electric field (Figure 2a). The Coulomb trap ionization probability has the following form [26,27]:

$$P = \nu \exp \left(- \frac{W - \left(\frac{e^3}{\pi \epsilon_\infty \epsilon_0} \right)^{1/2} \sqrt{\frac{U}{d}}}{kT} \right), \tag{4}$$

where $\nu = W/h$ —attempt to escape factor, W —trap ionization energy.

The H-A model describes the charge transport mechanism through overlapping Coulomb traps. In the H-A model, the trap ionization probability is described by the following equation (Figure 2b) [28,29]:

$$P = 2\nu \exp \left(- \frac{W - \frac{e^2}{\pi \epsilon_\infty \epsilon_0 s}}{kT} \right) \sinh \left(\frac{e \frac{U}{d} s}{2kT} \right) \tag{5}$$

According to the ME-L model, the charge transport in a dielectric is controlled by the multiphonon isolated trap ionization (Figure 2c) [30]. The current density is described by Equation (3), and the trap ionization probability in the ME-L model is described by Equations (6) and (7) [30]:

$$P = \sum \exp \left(\frac{nW_{ph}}{2kT} - \frac{W_{opt} - W_t}{W_{ph}} \coth \frac{nW_{ph}}{2kT} \right) I_n \left(\frac{W_{opt} - W_t}{W_{ph} \sinh(W_{ph}/2kT)} \right) P_i(W_t + nW_{ph}) \tag{6}$$

$$P_i = \frac{e \times \left(\frac{U}{d} \right)}{2\sqrt{2m^*W}} \exp \left(- \frac{4}{3} \frac{\sqrt{2m^*}}{\hbar e \times \left(\frac{U}{d} \right)} W^{3/2} \right) \tag{7}$$

where W_t —thermal trap energy, W_{opt} —optical trap energy, W_{ph} —phonon energy, I_n —modified Bessel function, P_i —tunneling probability through a triangular barrier, and $\hbar = h/2\pi$ —reduced Plank constant.

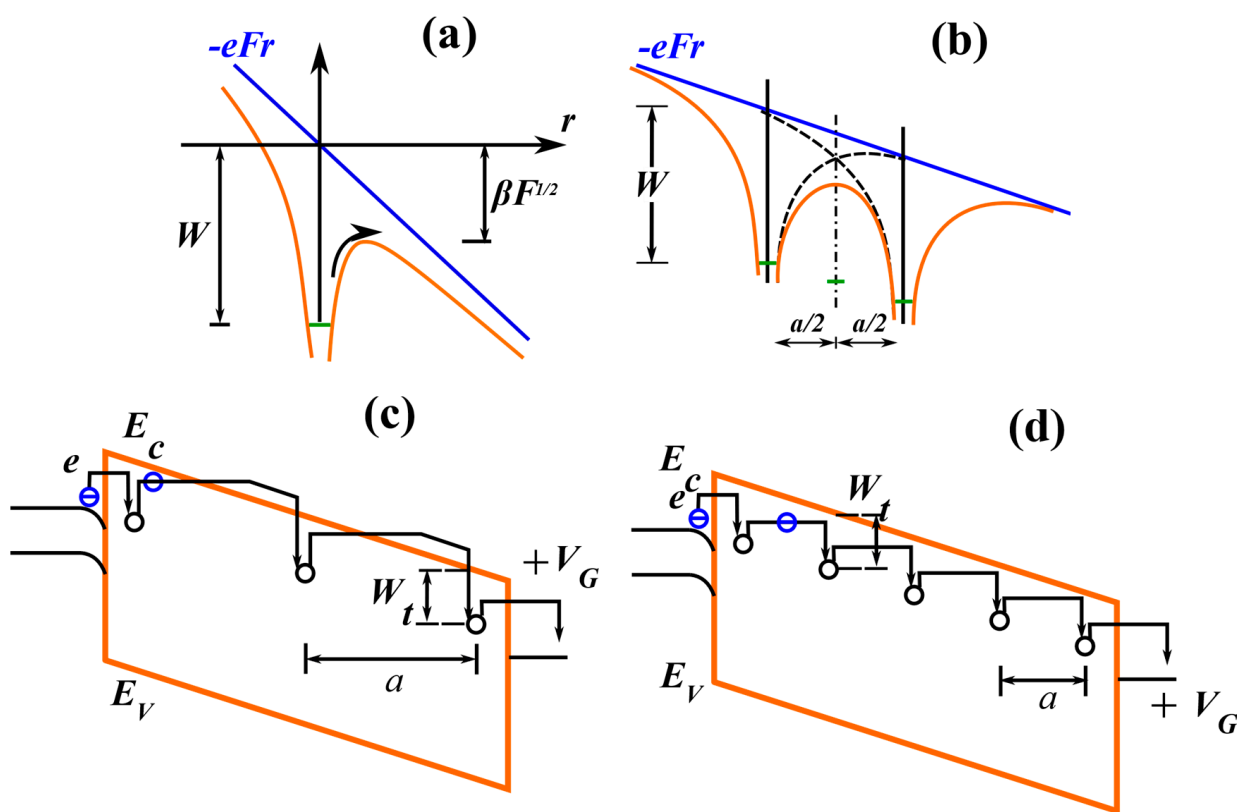


Figure 2. Schematic diagram of bulk-limited models: (a) Frenkel effect, (b) Hill–Adachi model of overlapping Coulomb potentials, (c) Makram–Ebeid and Lannoo multiphonon isolated trap ionization model, (d) Nasyrov–Gritsenko phonon-assisted tunneling via neighboring traps model.

The electron is excited from the ground state with the multiphonon absorption, and it tunnels to a neighboring trap due to a large integral overlapping value in the N-G model (Figure 2d). In the N-G model, the trap ionization probability is given by the following equation [31]:

$$P = \frac{2\sqrt{\pi}\hbar W_t}{m^*s^2\sqrt{2kT(W_{opt} - W_t)}} \exp\left(-\frac{W_{opt} - W_t}{kT}\right) \exp\left(-\frac{2s\sqrt{2m^*W_t}}{\hbar}\right) \sinh\left(\frac{eU_d s}{2kT}\right) \quad (8)$$

The charge transport in a non-stoichiometric dielectric can be described according to the S-E percolation model [32,33]. This model assumes that excited electrons with an energy higher than the percolation energy W_e are delocalized, and, moving round a random potential, they transfer the charge. The current–voltage characteristics have the following form [32,33]:

$$I = I_0 \exp\left(-\frac{W_e - \left(Ce\frac{U_d}{d}aV_0^\gamma\right)^{\frac{1}{1+\gamma}}}{kT}\right), \quad (9)$$

where I_0 is the pre-exponential factor, W_e is the percolation energy, a is the space scale of fluctuations, V_0 is the energy fluctuation amplitude, $C \approx 0.25$ is a numeric constant, and γ is the critical index and is equal to 0.9.

The theory of SCLC between flat parallel electrodes is presented in detail in [37]. The current in the SCLC model consists of several sections with different current–voltage

dependences. In our case, there are Ohmic and quadratic parts, which are given by the following expressions:

$$I = I_{\text{Ohm}} + I_{\text{SCLC}} = Se\mu n \frac{U}{d} + S \frac{9}{8} \mu \varepsilon \varepsilon_0 \theta \frac{U^2}{d^3}, \quad (10)$$

$$n = \frac{2N_d}{1 + \sqrt{1 + \frac{4gN_d}{N_c} \exp\left(\frac{E_a}{kT}\right)}}; N_c = 2 \left(\frac{2\pi m^* kT}{h^2} \right)^{\frac{3}{2}}; \theta = \frac{N_c}{N_t} \exp\left(\frac{-W_t}{kT}\right); \quad (11)$$

where S is the area involved in the charge transport, μ is electron mobility, n is free electron concentration in the dielectric, ε is static dielectric constant, θ is the fraction of free electrons from all injected ones (trapped and free), N_d is donor concentration, g is degeneracy factor, N_c is effective density of states, E_a is donor activation energy, N_t is trap concentration, W_t is trap energy, m^* is electron effective mass, and h is the Planck constant.

If we have the third part in the SCLC model not proportional to the square, we will use the following SCLC formula [37]:

$$I = Se\mu n \frac{U}{d} + S \frac{9}{8} \mu \varepsilon \varepsilon_0 \theta \frac{U^2}{d^3} + SN_c \mu e^{1-l} \left(\frac{\varepsilon l}{N_c(l+1)} \right)^l \left(\frac{2l+1}{l+1} \right)^{l+1} \frac{U^{l+1}}{d^{2l+1}} \quad (12)$$

where $l = T_t/T$, and T_t is the temperature parameter that characterizes the exponential trap distribution.

To compare the theoretical charge transport models and the temperature IV characteristics, we used the method of least absolute deviations [38]. Most theoretical models are described in the logarithmic form ($\text{Log } J \sim U$ or $J \sim e^U$); in addition, most IV characteristics are also described in the form of $\text{Log } J \sim U$. Therefore, we used the absolute deviation as per the following formula:

$$\Delta_{\text{max}} = \left| \text{Log} \frac{J_{\text{theory}}}{J_{\text{experiment}}} \right| \times 100\% \quad (13)$$

The method of least absolute deviations was applied until the absolute deviation of the theoretical maximum current value from the experiment was 20% or less.

To model the experimental data, we used only the analytical calculation using Mathematica software. To conduct a more accurate simulation, we needed to account for the local field distribution in the sample with the Poisson equation and Shockley–Read–Hall statistics for the trap occupation. However, that required more specialized and complex software for numerical calculation.

3. Results and Discussion

The IV characteristics of the obtained PECVD SiO_{0.9}N_{0.6}-based memristor structures and their switching were investigated. The switching cycles for a PECVD SiO_{0.9}N_{0.6}-based memristor are shown in Figure 3. There were only two states: HRS and LRS. The PECVD SiO_{0.9}N_{0.6}-based memristor in the initial state (before forming) was in the LRS. Hence, the PECVD SiN_xO_y-based memristor did not require forming, which is an advantage, compared to memristors based on PECVD SiO_x:H [9] and PECVD SiN_x:H [10]. The memristors based on PECVD SiO_x:H [9] and PECVD SiN_x:H [10] have a unique forming process: the forming process does not require high voltages for the first switch, and the initial state in those memristors has a smaller resistance than that of LRS; however, after the first cycle, we cannot return to the initial state. Therefore, the memristors based on PECVD SiO_x:H and PECVD SiN_x:H need a forming stage, but they do not require high voltages for the forming cycle, which avoids the memory cell breakdown.

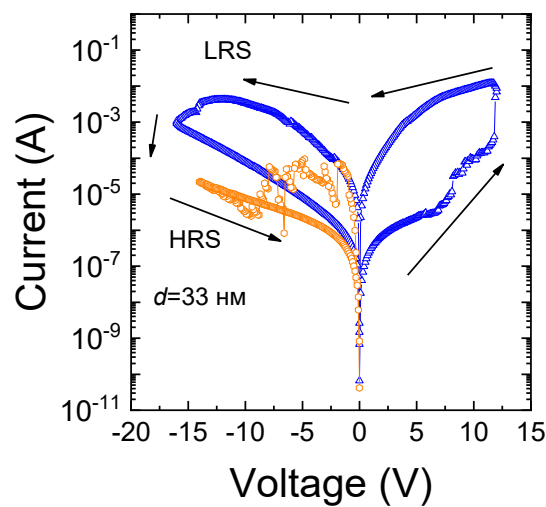


Figure 3. IV characteristics of the PECVD SiO_{0.9}N_{0.6}-based memristor.

3.1. Contact-Limited Charge Transport Mechanism in the PECVD SiO_{0.9}N_{0.6}-Based Memristor

The IV characteristics of the PECVD SiO_{0.9}N_{0.6}-based memristor in the HRS and LRS were simulated by contact-limited charge transport models. The Schottky effect and thermally assisted tunneling (TAT) model qualitatively were used to describe the IV characteristics of the PECVD SiN_xO_y-based memristor in the LRS (Figure 4a) and HRS (Figure 4c). However, the Schottky effect predicted an abnormally small effective mass value for the PECVD SiN_xO_y-based memristor (for the LRS $m^* = 2.3 \times 10^{-5} m_e$ and for the HRS $m^* = 1 \times 10^{-12} m_e$). The Schottky effect also gave an abnormally larger high-frequency dielectric constant value for the PECVD SiN_xO_y-based memristor (for the LRS $\epsilon_\infty = 18$ and for the HRS $\epsilon_\infty = 9$). The TAT model did not describe the charge transport mechanism because when modelling the experimental data, it obtained abnormally small values for the transport area for the PECVD SiN_xO_y-based memristor (for the LRS $S = 4 \times 10^{-16} \text{ m}^2$ and for the HRS $S = 1.0 \times 10^{-14} \text{ m}^2$). In addition, the barrier energies for the Schottky effect and TAT model were 0.15 eV for the LRS and HRS. Those energies represent the barrier energies at the Si/SiO_{0.9}N_{0.6} interface. In [20], we estimated the energy gap as 4.1 eV for this memristor structure. Thus, the barrier energies at the Si/SiO_{0.9}N_{0.6} interface for an electron and a hole, at least, will be around 1 eV or more in the HRS.

3.2. Bulk-Limited Charge Transport Mechanism in the PECVD SiO_{0.9}N_{0.6}-Based Memristor

In the memristor, the HRS conduction filament is partially or fully disrupted. In that case, conduction in the HRS is similar to dielectric conduction. Thin dielectric film conductivity can be divided into two processes: charge-carrier injection from the contact into the dielectric, and charge transport in the dielectric bulk. Because current depends on temperature, we excluded the Fowler–Nordheim model [39]. If there is a high trap concentration in the dielectric, then the space charge on them limits the injection from the contact, and the leakage current is limited by the trap ionization rate. The trap ionization can be described by six analytical bulk-limited current models.

The experimental charge transport simulation data with the Frenkel effect for the PECVD SiO_{0.9}N_{0.6}-based memristor in the LRS and in HRS are shown in Figures 5a and 6a. From the current temperature dependence, we found that the trap ionization energy was 0.13 eV. The attempt to escape factor controls the vertical position of the theoretical IV characteristic, and it can be found from the trap ionization energy with formula $\nu = W/h = 3.1 \times 10^{13} \text{ s}^{-1}$. The trap concentration parameter in the Frenkel model also governs the vertical theoretical curve position, and the high-frequency dielectric constant governs the slope of the theoretical curve. To describe the experimental data by the Frenkel effect, we obtained the abnormally low trap concentration value for the PECVD SiO_{0.9}N_{0.6}-based memristor (for the LRS $N = 8 \times 10^6 \text{ cm}^{-3}$ and for the HRS $N = 100 \text{ cm}^{-3}$) and the

abnormally large high-frequency dielectric constant value for the PECVD SiO_{0.9}N_{0.6}-based memristor in both states (for the LRS $\epsilon_\infty = 65$ and for the HRS $\epsilon_\infty = 28$).

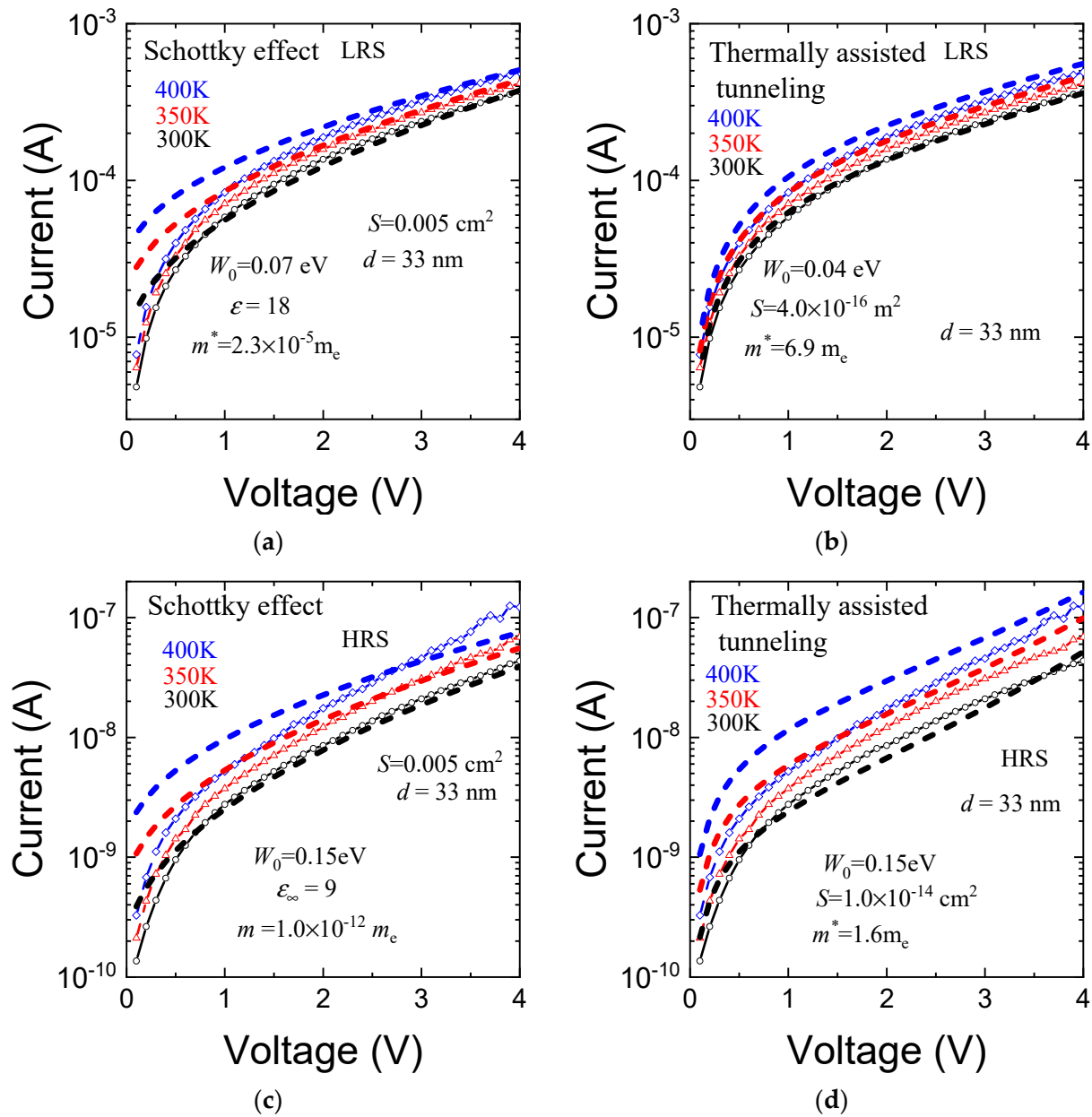


Figure 4. The IV characteristics of the PECVD SiO_{0.9}N_{0.6}-based memristor and simulation results by the contact-limited models: (a) Schottky effect in LRS; (b) the TAT model in LRS; (c) the Schottky effect in HRS; and (d) the TAT model in HRS.

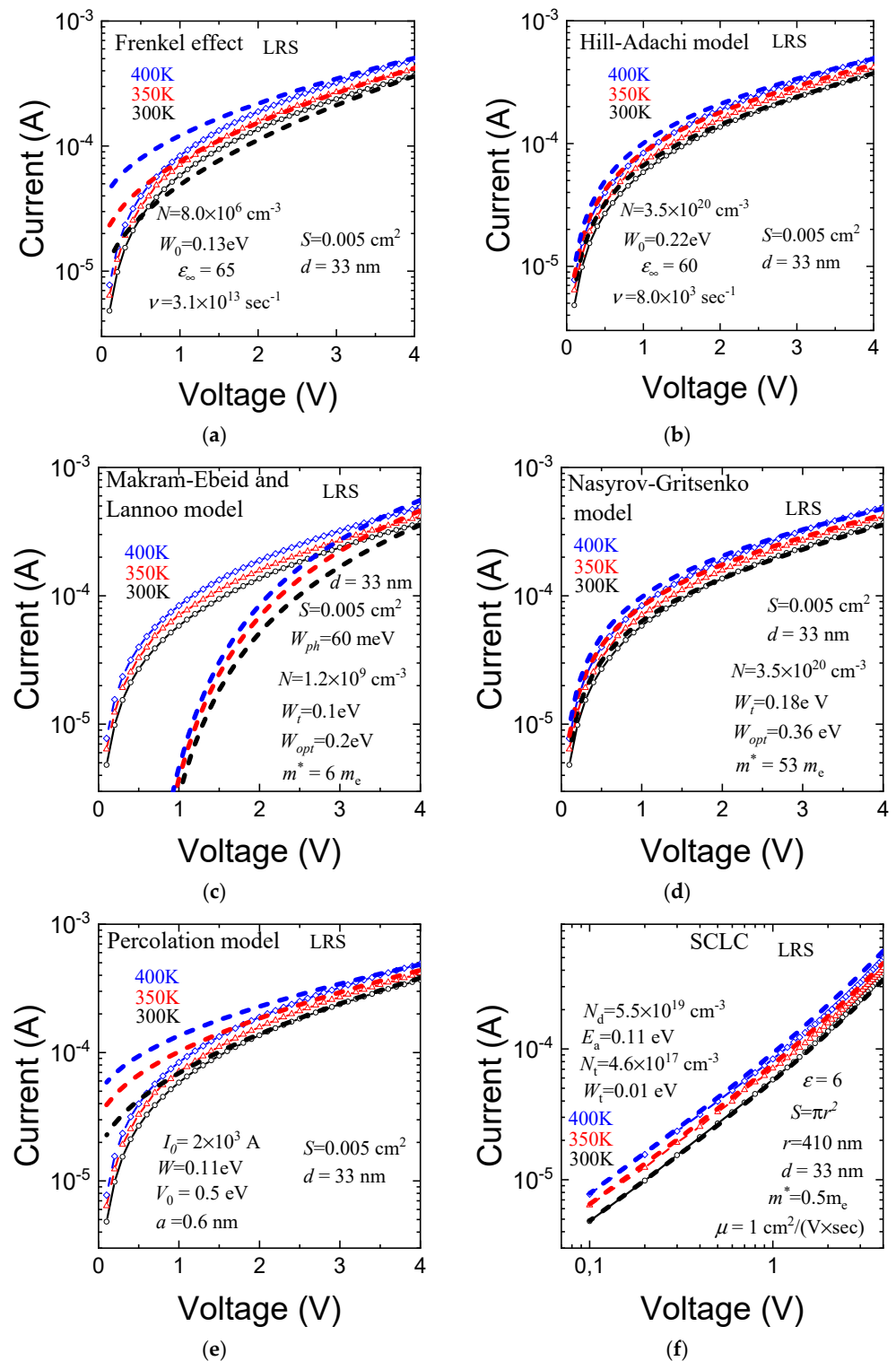


Figure 5. IV characteristics of the PECVD SiO_{0.9}N_{0.6}-based memristor and the results of simulation by the bulk-limited models in the HRS: (a) Frenkel effect; (b) Hill–Adachi model of overlapping Coulomb potentials; (c) Makram–Ebeid and Lannoo model of multiphonon isolated trap ionization; (d) Nasyrov–Gritsenko model of phonon-assisted tunneling between traps; (e) Shklovskii–Efros percolation model; and (f) SCLC model.

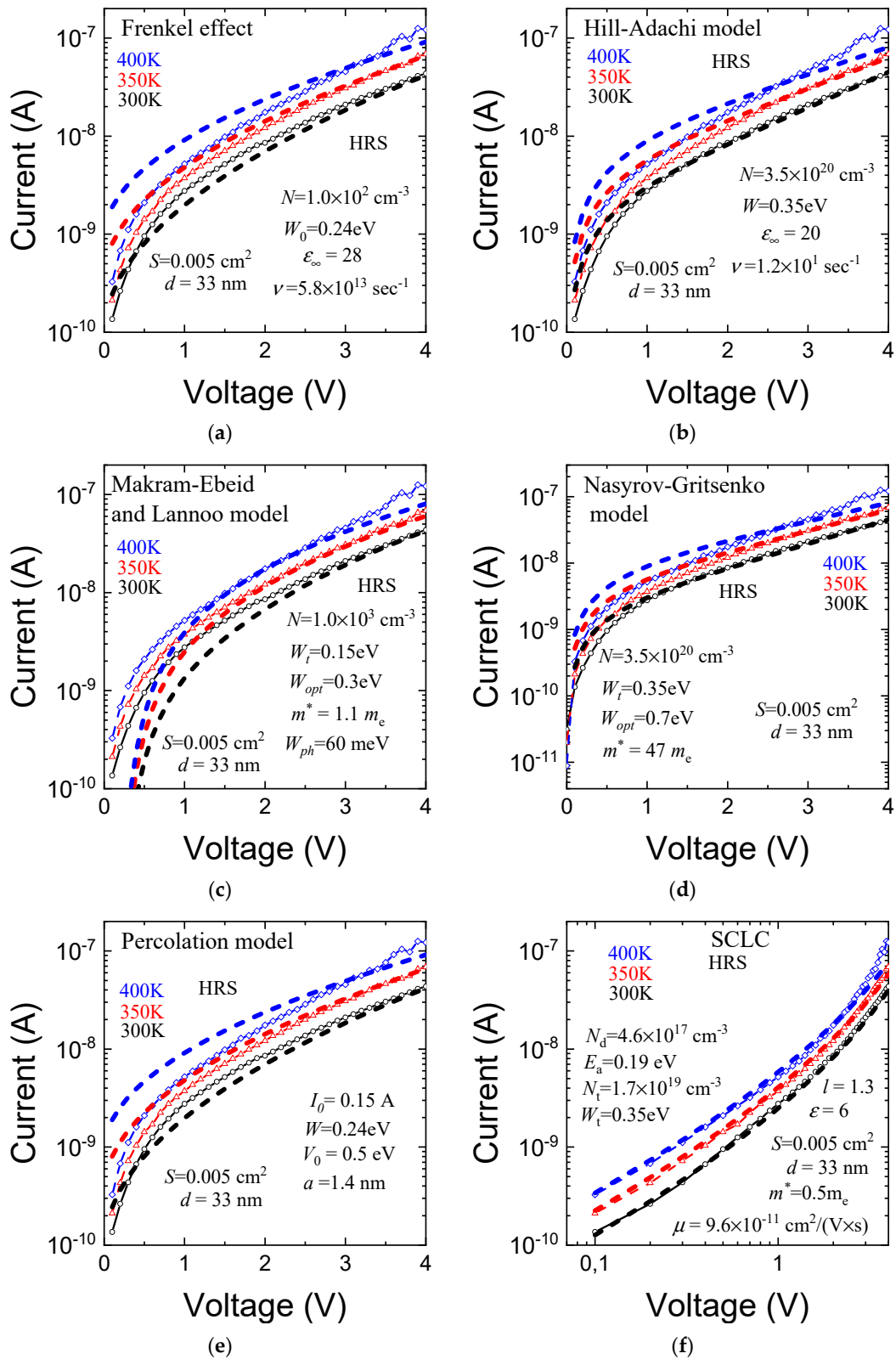


Figure 6. IV characteristics of the PECVD SiO_{0.9}N_{0.6}-based memristor, and the results of simulation by the bulk-limited models in HRS: (a) Frenkel effect; (b) Hill–Adachi model of overlapping Coulomb potentials; (c) Makram–Ebeid and Lannoo multiphonon isolated trap ionization model; (d) Nasyrov–Gritsenko model of phonon-assisted tunneling between traps, (e) Shklovskii–Efros percolation model; and (f) the SCLC model.

The IV characteristics of the PECVD SiO_{0.9}N_{0.6}-based memristor and the results of the simulation by the H-A model are shown in Figures 5b and 6b. The H-A model describes the charge transport when Coulomb traps overlap; the overlapping happens when the distance between traps is small. Therefore, the trap concentration is large. Hence, we could use the H-A model to obtain an accurate estimate of the trap concentration value (for the LRS— $N = 3.5 \times 10^{20} \text{ cm}^{-3}$ and for the HRS— $N = 3.5 \times 10^{20} \text{ cm}^{-3}$). The attempt to escape factor could be found with the same formula as in the Frenkel model. Moreover, with the trap ionization energies $W = 0.22 \text{ eV}$ for the LRS and $W = 0.35 \text{ eV}$ for the HRS, the theoretical attempt to escape factor values were $\nu = 5.3 \times 10^{13} \text{ s}^{-1}$ for the LRS and $\nu = 8.5 \times 10^{13} \text{ s}^{-1}$ for the HRS. However, to describe the experimental data, the H-A model predicts the abnormally small attempt to escape factor values (for the LRS— $\nu = 8 \times 10^3 \text{ s}^{-1}$ and for the HRS— $\nu = 1.2 \times 10^1 \text{ s}^{-1}$) for the PECVD SiO_{0.9}N_{0.6}-based memristor in both states. In addition, the abnormally large high-frequency dielectric constant value for the PECVD SiO_{0.9}N_{0.6}-based memristor in both states is predicted by the H-A model (for the LRS— $\epsilon_\infty = 60$ and for the HRS— $\epsilon_\infty = 20$). Thus, the H-A model does not describe the charge transport mechanism in the PECVD SiO_{0.9}N_{0.6}-based memristor.

The ME-L model describes the multiphonon ionization of isolated traps. When we modeled the experimental data with this model, we obtained reasonable thermal trap ionization energy, optical trap ionization energy, and effective mass values (Figures 5c and 6c). However, in the ME-L model, the trap concentration value was predicted to be abnormally small (for the LRS— $N = 1.2 \times 10^9 \text{ cm}^{-3}$ and for the HRS— $N = 1.0 \times 10^3 \text{ cm}^{-3}$). In addition, for the LRS, even with those reasonable parameters, the ME-L model described the experimental data only at high voltages. Therefore, the ME-L model did not describe the charge transport mechanism in the PECVD SiO_{0.9}N_{0.6}-based memristor in any states.

The IV characteristics of the PECVD SiO_{0.9}N_{0.6}-based memristor and results of simulation by the N-G model are shown in Figures 5d and 6d. The N-G model is similar to H-A model and describes the charge transport mechanism at a high trap concentration, and the N-G model predicts the same trap concentration as in the H-A model (for the LRS— $N = 3.5 \times 10^{20} \text{ cm}^{-3}$ and for the HRS— $N = 3.5 \times 10^{20} \text{ cm}^{-3}$). It is the same value because the N-G model and the H-A model govern the same theoretical slope and vertical position as in another model. However, the N-G model did not describe the charge transport mechanism, since quantitative agreement of the experimental data and the theoretical models was reached with the abnormally large effective mass value for the PECVD SiO_{0.9}N_{0.6}-based memristor (for the LRS— $m^* = 47 m_e$ and for the HRS— $m^* = 9.2 m_e$).

For the S-E percolation model, the resulting fluctuation space scale was about 0.6 nm for the LRS and 1.4 nm for the HRS for the PECVD SiO_{0.9}N_{0.6}-based memristor (Figures 5e and 6e). Since the tunneling probability at such spatial scales was high, the classical approximation criterion of the S-E model applicability was not fulfilled. Thus, the S-E percolation model could not be used to describe the charge transport mechanism in the PECVD SiO_{0.9}N_{0.6}-based memristor in any states.

To apply the SCLC model, we did not account for the switching process. In the classical SCLC, an increase in current is related to filling traps, but in the memristor switching process, it is very complex and is usually related to creating and destroying a conduction channel. Thus, the SCLC cannot be applied to bipolar memristors. The SCLC can only be applied individually to the LRS or HRS without the switching process. To account for the differences in memristor states, we introduced the filament size changes from state to state. We did not account for the conductive filament thickness changes, although in the HRS the conductive channel can dissolve partially or completely. In addition, we did not take into account the possibility of structural changes in the conductive channel during the resistance switching. With those assumptions, the current in the LRS and in HRS for the PECVD SiO_{0.9}N_{0.6}-based memristor was described by the SCLC model (Figures 5f and 6f). There are many variable parameters in the SCLC model. The effective mass was taken as $m^* = 0.5 m_e$, and the static dielectric constant value was taken as 6 for

$\text{SiO}_{0.9}\text{N}_{0.6}$. The simulation of the experimental IV characteristics in the LRS for the PECVD $\text{SiO}_{0.9}\text{N}_{0.6}$ -based memristor showed that the effective conducting channel diameter of was 820 nm, the donor defect ionization energy was 0.11 eV, the donor defect concentration was $5.5 \times 10^{19} \text{ cm}^{-3}$, the trap ionization energy was 0.01 eV, and the trap concentration was $4.6 \times 10^{17} \text{ cm}^{-3}$. The simulation of the experimental IV characteristics in the HRS for the PECVD $\text{SiO}_{0.9}\text{N}_{0.6}$ -based memristor gave the following results: the conductivity spanned the entire contact area ($S = 0.005 \text{ cm}^2$), the donor defect ionization energy was 0.19 eV, the donor defect concentration was $4.6 \times 10^{17} \text{ cm}^{-3}$, the trap ionization energy was 0.35 eV, and the trap concentration was $1.7 \times 10^{19} \text{ cm}^{-3}$. In the HRS, there was a third section of SCLC with a degree of 2.3. The Tables A1 and A2 in Appendix A show all fitted parameters in all applied models.

The SCLC characteristics were significantly different from those of the experimentally observed in the HRS at 400 K from the 3 V to the 4 V part of the curve. This difference was due to the pre-switching portion of the IV curve, which was similar to the IV curve in Figure 3 from 6 V to 8 V. At a higher temperature, the switching began at a low voltage, as shown in Figure 6f. We simulated the IV curves only at a fixed resistance. However, at this pre-switching portion, the resistance began to change. Thus, we did not include it in the simulation.

4. Conclusions

The IV characteristics of the obtained PECVD $\text{SiO}_{0.9}\text{N}_{0.6}$ -based memristor structures and their switching revealed that the PECVD $\text{SiO}_{0.9}\text{N}_{0.6}$ -based memristor is forming-free. To clarify the charge transport mechanism in the PECVD $\text{SiO}_{0.9}\text{N}_{0.6}$ -based forming-free memristor, the current at different temperature values in the high resistance state and low resistance states was simulated by the Schottky effect, the thermally assisted tunneling model, the Frenkel effect model of Coulomb isolated trap ionization, the Hill–Adachi model of overlapping Coulomb potentials, the Makram–Ebeid and Lannoo multiphonon isolated trap ionization model, the Nasyrov–Gritsenko model of phonon-assisted tunneling between traps, the Shklovskii–Efros percolation model, and the space-charge limited current model. After filtering out the models by various fitted parameters, the charge transport mechanism in the forming-free PECVD SiO_xN_y -based memristor in the high and low resistance states could be described by the space-charge-limited current model. The trap ionization energy $W_t = 0.35 \text{ eV}$ and the trap concentration $N_d = 1.7 \times 10^{19} \text{ cm}^{-3}$ were obtained from simulation using the SCLC model in the high resistance state. For the low resistance state, the trap ionization energy was $W_t = 0.01 \text{ eV}$, and the trap concentration was $N_t = 4.6 \times 10^{17} \text{ cm}^{-3}$.

Author Contributions: Conceptualization, V.A.G. and V.A.V.; methodology, V.A.G., A.A.G. and G.N.K.; validation, V.A.G., V.A.V. and A.A.G.; formal analysis, A.A.G.; investigation, A.A.G.; resources, G.N.K.; writing—original draft preparation, A.A.G. and V.A.V.; writing—review and editing, A.A.G. and V.A.V.; visualization, A.A.G.; supervision, V.A.G. and V.A.V.; project administration, V.A.G. and V.A.V.; funding acquisition, V.A.V. All authors have read and agreed to the published version of the manuscript.

Funding: This research was funded by the Russian Science Foundation, grant number 22-19-00369.

Acknowledgments: The work was supported by the Russian Science Foundation, project No. 22-19-00369. The electrophysical measurements were conducted using equipment from the Center of Collective Usage “VTAN” NSU supported by the Ministry of Education and Science of Russia by agreement #075-12-2021-697.

Conflicts of Interest: The authors declare no conflict of interest. The funders had no role in the design of the study; in the collection, analyses, or interpretation of data; in the writing of the manuscript; or in the decision to publish the results.

Appendix A

Table A1. Constant and fitted parameters of the Schottky effect, TAT model, Frenkel effect, and H-A model. The bold and underline parameters are parameters due to which the model does not fit experimental data.

State	Schottky Effect	TAT	Frenkel Effect	H-A Model
LRS	Constant: $S = 0.005 \text{ cm}^2 *$ $d = 33 \text{ nm}$ Fitted: $W_0 = 0.07 \text{ eV}$ $\epsilon_\infty = 18$ $m^* = 2.3 \times 10^{-5} m_e$	Constant: $d = 33 \text{ nm}$ Fitted: $W_0 = 0.04 \text{ eV}$ $S = 4 \times 10^{-16} \text{ m}^2$ $m^* = 6.9 m_e$	Constant: $S = 0.005 \text{ cm}^2 *$ $d = 33 \text{ nm}$ Fitted: $W = 0.13 \text{ eV}$ $\nu = 3.1 \times 10^{13} \text{ s}^{-1}$ $\epsilon_\infty = 65$ $N = 8.0 \times 10^6 \text{ cm}^{-3}$	Constant: $S = 0.005 \text{ cm}^2 *$ $d = 33 \text{ nm}$ Fitted: $N = 3.5 \times 10^{20} \text{ cm}^{-3}$ $W = 0.22 \text{ eV}$ $\epsilon_\infty = 60$ $\nu = 8.0 \times 10^3 \text{ s}^{-1}$
HRS	Constant: $S = 0.005 \text{ cm}^2$ $d = 33 \text{ nm}$ Fitted: $W_0 = 0.15 \text{ eV}$ $\epsilon_\infty = 9$ $m^* = 1.0 \times 10^{-12} m_e$	Constant: $S = 0.005 \text{ cm}^2$ $d = 33 \text{ nm}$ Fitted: $W_0 = 0.15 \text{ eV}$ $S = 1.0 \times 10^{-14} \text{ m}^2$ $m^* = 1.4 m_e$	Constant: $S = 0.005 \text{ cm}^2$ $d = 33 \text{ nm}$ Fitted: $W = 0.24 \text{ eV}$ $\nu = 5.8 \times 10^{13} \text{ sec}^{-1}$ $\epsilon_\infty = 28$ $N = 1.0 \times 10^2 \text{ cm}^{-3}$	Constant: $S = 0.005 \text{ cm}^2$ $d = 33 \text{ nm}$ Fitted: $N = 3.5 \times 10^{20} \text{ cm}^{-3}$ $W = 0.35 \text{ eV}$ $\epsilon_\infty = 20$ $\nu = 1.2 \times 10^1 \text{ s}^{-1}$

* Area is a fitted parameter in the LRS, but the modeling had been stopped due to other parameters before the area parameter could be determined.

Table A2. Constant and fitted parameters of the ME-L model, N-G model, S-E model, and SCLC model. The bold and underline parameters are parameters due to which the model does not fit experimental data.

State	ME-L Model	N-G Model	S-E Model	SCLC
LRS	Constant: $S = 0.005 \text{ cm}^2 *$ $d = 33 \text{ nm}$ Fitted: $N = 1.2 \times 10^9 \text{ cm}^{-3}$ $W_t = 0.1 \text{ eV}$ $W_{opt} = 0.2 \text{ eV}$ $W_{ph} = 60 \text{ meV}$ $m^* = 6 m_e$	Constant: $S = 0.005 \text{ cm}^2 *$ $d = 33 \text{ nm}$ Fitted: $N = 3.5 \times 10^{20} \text{ cm}^{-3}$ $W_t = 0.18 \text{ eV}$ $W_{opt} = 0.36 \text{ eV}$ $m^* = 53 m_e$	Constant: $S = 0.005 \text{ cm}^2 *$ $d = 33 \text{ nm}$ Fitted: $I_0 = 2 \times 10^3 \text{ A}$ $W = 0.11 \text{ eV}$ $V_0 = 0.5 \text{ eV}$ $a = 0.6 \text{ nm}$	Constant: $\epsilon = 6$ $d = 33 \text{ nm}$ $m^* = 0.5 m_e$ $\mu = 1 \text{ cm}^2 / (\text{V} \times \text{s})$ Fitted: $E_a = 0.11 \text{ eV}$ $N_d = 5.5 \times 10^{19} \text{ cm}^{-3}$ $W_t = 0.01 \text{ eV}$ $N_t = 4.6 \times 10^{17} \text{ cm}^{-3}$ $r = 410 \text{ nm}$
HRS	Constant: $S = 0.005 \text{ cm}^2$ $d = 33 \text{ nm}$ Fitted: $N = 1.0 \times 10^3 \text{ cm}^{-3}$ $W_t = 0.15 \text{ eV}$ $W_{opt} = 0.3 \text{ eV}$ $W_{ph} = 60 \text{ meV}$ $m^* = 1.1 m_e$	Constant: $S = 0.005 \text{ cm}^2$ $d = 33 \text{ nm}$ Fitted: $N = 3.5 \times 10^{20} \text{ cm}^{-3}$ $W_t = 0.35 \text{ eV}$ $W_{opt} = 0.7 \text{ eV}$ $m^* = 47 m_e$	Constant: $S = 0.005 \text{ cm}^2$ $d = 33 \text{ nm}$ Fitted: $I_0 = 0.15 \text{ A}$ $W = 0.24 \text{ eV}$ $V_0 = 0.5 \text{ eV}$ $a = 1.4 \text{ nm}$	Constant: $S = 0.005 \text{ cm}^2$ $d = 33 \text{ nm}$ $\epsilon = 6$ $m^* = 0.5 m_e$ Fitted: $E_a = 0.19 \text{ eV}$ $N_d = 4.6 \times 10^{17} \text{ cm}^{-3}$ $W_t = 0.35 \text{ eV}$ $N_t = 1.7 \times 10^{19} \text{ cm}^{-3}$ $l = 1.3$ $\mu = 9.6 \times 10^{-11} \text{ cm}^2 / (\text{V} \times \text{s})$

* Area is a fitted parameter in the LRS, but the modeling had been stopped due to other parameters before the area parameter could be determined.

References

1. Shi, Y.; He, L.; Guang, F.; Li, L.; Xin, Z.; Liu, R. A Review: Preparation, Performance, and Applications of Silicon Oxynitride Film. *Micromachines* **2019**, *10*, 552. [CrossRef]
2. Strukov, D.B.; Snider, G.S.; Stewart, D.R.; Williams, R.S. The missing memristor found. *Nature* **2008**, *453*, 80–83. [CrossRef] [PubMed]
3. Lee, M.J.; Lee, C.; Lee, D.; Chang, M.; Hur, J.H.; Kim, Y.-B.; Kim, C.-J.; Seo, D.H.; Seo, S.; Chung, U.-I.; et al. A fast, high-endurance and scalable non-volatile memory device made from asymmetric Ta₂O_{5-x}/TaO_{2-x} bilayer structures. *Nature Mater.* **2011**, *10*, 625–630. [CrossRef]
4. Prakash, A.; Jana, D.; Maikap, S. TaOx-based resistive switching memories: Prospective and challenges. *Nanoscale Res. Lett.* **2013**, *8*, 418. [CrossRef]
5. Mezziani, S.; Moussi, A.; Mahiou, L.; Outemzabet, R. Compositional analysis of silicon oxide/silicon nitride thin films. *Mater. Sci.* **2016**, *34*, 315–321. [CrossRef]
6. Iwase, Y.; Horie, Y.; Daiko, Y.; Honda, S.; Iwamoto, Y. Synthesis of a Novel Polyethoxysilsesquiazane and Thermal Conversion into Ternary Silicon Oxynitride Ceramics with Enhanced Thermal Stability. *Materials* **2017**, *10*, 1391. [CrossRef]
7. Mehonic, A.; Shluger, A.L.; Gao, D.; Valov, I.; Miranda, E.; Ielmini, D.; Bricalli, A.; Ambrosi, E.; Li, C.; Yang, J.J.; et al. Silicon oxide (SiOx): A promising material for resistance switching? *Adv. Mater.* **2018**, *30*, 1801187. [CrossRef] [PubMed]
8. Yao, J.; Zhong, L.; Natelson, D.; Tour, J.M. Silicon oxide: A non-innocent surface for molecular electronics and nanoelectronics studies. *J. Am. Chem. Soc.* **2011**, *133*, 941. [CrossRef]
9. Gismatulin, A.A.; Voronkovskii, V.A.; Kamaev, G.N.; Novikov, Y.N.; Kruchinin, V.N.; Krivyakin, G.K.; Gritsenko, V.A.; Prosvirin, I.P.; Chin, A. Electronic structure and charge transport mechanism in a forming-free SiOx-based memristor. *Nanotechnology* **2020**, *31*, 505704. [CrossRef]
10. Gismatulin, A.A.; Kamaev, G.N.; Kruchinin, V.N.; Gritsenko, V.A.; Orlov, O.M.; Chin, A. Charge transport mechanism in the forming-free memristor based on silicon nitride. *Sci. Rep.* **2021**, *11*, 2417.
11. Winn, E.B. The Temperature Dependence of the Self-Diffusion Coefficients of Argon, Neon, Nitrogen, Oxygen, Carbon Dioxide, and Methane. *Phys. Rev.* **1950**, *80*, 1024–1027. [CrossRef]
12. Kijima, K.; Shirasaki, S. Nitrogen self-diffusion in silicon nitride. *J. Chem. Phys.* **1976**, *65*, 2668–2671. [CrossRef]
13. Roussel, M.; Talbot, E.; Pareige, P.; Gourbilleau, F. Influence of the supersaturation on Si diffusion and growth of Si nanoparticles in silicon-rich silica. *J. Appl. Phys.* **2013**, *113*, 063519. [CrossRef]
14. Volodin, V.A.; Geydt, P.; Kamaev, G.N.; Gismatulin, A.A.; Krivyakin, G.K.; Prosvirin, I.P.; Azarov, I.A.; Fan, Z.; Vergnat, M. Resistive Switching in Non-Stoichiometric Germanosilicate Glass Films Containing Ge Nanoclusters. *Electronics* **2020**, *9*, 2103. [CrossRef]
15. Chen, D.; Huang, S.; He, L. Effect of oxygen concentration on resistive switching behavior in silicon oxynitride film. *J. Semicond.* **2017**, *38*, 043002. [CrossRef]
16. Vasileiadis, N.; Karakolis, P.; Mandylas, P.; Ioannou-Souglideris, V.; Normand, P.; Perego, M.; Komninou, P.; Ntinias, V.; Fyrigos, I.-A.; Karafyllidis, I.; et al. Understanding the role of defects in silicon nitride-based resistive switching memories through oxygen doping. *IEEE Trans. Nanotechnol.* **2021**, *20*, 365. [CrossRef]
17. Leng, K.; Zhu, X.; Ma, Z.; Yu, X.; Xu, J.; Xu, L.; Li, W.; Chen, K. Artificial neurons and synapses based on Al/a-SiN_xO_y:H/P+-Si device with tunable resistive switching from threshold to memory. *Nanomaterials* **2022**, *12*, 311. [CrossRef]
18. Yu, Z.; Aceves, M.; Carrillo, J.; Lopez-Estopier, R. Charge trapping and carrier transport mechanism in silicon-rich silicon oxynitride. *Thin Solid Films* **2006**, *515*, 2366–2372. [CrossRef]
19. Yonamoto, Y.; Inaba, Y.; Akamatsu, N. Compositional dependence of trap density and origin in thin silicon oxynitride film investigated using spin dependent Poole–Frenkel current. *Appl. Phys. Lett.* **2011**, *98*, 232905. [CrossRef]
20. Novikov, Y.N.; Gismatulin, A.A.; Prosvirin, I.P.; Bobovnikov, P.G.; Krasnikov, G.Y.; Gritsenko, V.A. Short-range order and charge transport in silicon-rich pyrolytic silicon oxynitride. *J. Non Cryst. Solids* **2023**, *599*, 121984. [CrossRef]
21. Perevalov, T.V.; Volodin, V.A.; Kamaev, G.N.; Gismatulin, A.A.; Cherkova, S.G.; Prosvirin, I.P.; Astankova, K.N.; Gritsenko, V.A. Electronic structure of silicon oxynitride films grown by plasma-enhanced chemical vapor deposition for memristor application. *J. Non Cryst. Solids* **2022**, *598*, 121925. [CrossRef]
22. Antonenko, A.K.; Volodin, V.A.; Efremov, M.D.; Zazulya, P.S.; Kamaev, G.N.; Marin, D.V. Silicon nitride films deposited at substrate temperatures <100 °C in a permanent magnet electron cyclotron resonance plasma. *Optoelectron. Instrum. Data Process.* **2011**, *47*, 459.
23. Jensen, K.L. General formulation of thermal, field and photoinduced electron emission. *J. Appl. Phys.* **2007**, *102*, 024911. [CrossRef]
24. Roberts, G.G.; Polango, J.I. Thermally assisted tunneling in dielectric films. *Phys. Stat. Sol. a* **1970**, *1*, 409–420. [CrossRef]
25. Gritsenko, V.A.; Meerson, E.E.; Morokov, Y.N. Thermally assisted hole tunneling at the Au-Si₃N₄ interface and the energy-band diagram of metal-nitride-oxide-semiconductor structures. *Phys. Rev. B* **1998**, *57*, R2081–R2083. [CrossRef]
26. Frenkel, J. On the theory of electric breakdown of dielectrics and electronic semiconductors. *Tech. Phys. USSR* **1938**, *5*, 685–695.
27. Frenkel, J. On pre-breakdown phenomena in insulators and electronic semiconductors. *Phys. Rev. B* **1938**, *54*, 647. [CrossRef]
28. Hill, R.M. Poole-Frenkel conduction in amorphous solids. *Philos. Mag.* **1971**, *23*, 59–86. [CrossRef]
29. Adachi, H.; Shibata, Y.; Ono, S. On electronic conduction through evaporated silicon oxide films. *J. Phys. D Appl. Phys.* **1971**, *4*, 988–994. [CrossRef]

30. Makram-Ebeid, S.S.; Lannoo, M. Quantum model for phonon-assisted tunnel ionization of deep levels in a semiconductor. *Phys. Rev. B* **1982**, *25*, 6406. [[CrossRef](#)]
31. Nasyrov, K.A.; Gritsenko, V.A. Charge transport in dielectrics via tunneling between traps. *J. Appl. Phys.* **2011**, *109*, 093705. [[CrossRef](#)]
32. Shklovskii, B.I. Percolation Mechanism of Electrical-Conduction in Strong Electric-Fields. *Sov. Phys. Semicond.* **1979**, *13*, 53–56.
33. Shklovskii, B.I. & Efros, A.L. Percolation Theory and Conductivity of Highly Inhomogeneous-Media. *Usp. Fiz. Nauk.* **1975**, *117*, 401–435.
34. Mott, N.F.; Gurney, R.W. Electronic Processes in Ionic Crystals. *J. Phys. Chem.* **1941**, *45*, 1142.
35. Lampert, M.A. Simplified Theory of Space-Charge-Limited Currents in an Insulator with Traps. *Phys. Rev.* **1956**, *103*, 1648. [[CrossRef](#)]
36. Murgatroyd, P.N. Theory of space-charge-limited current enhanced by Frenkel effect. *J. Phys. D: Appl. Phys.* **1970**, *3*, 151–156. [[CrossRef](#)]
37. Lampert, M.A.; Mark, P. *Current Injection in Solids*; Academic Press: New York, USA, 1970; p. 351.
38. Bloomfield, P.; Steiger, W. *Least Absolute Deviations, Theory, Applications and Algorithms*; Huber, P., Rosenblatt, M., Eds.; Birkhäuser: Boston, MA, USA, 1983; p. 349.
39. Fowler, R.H.; Nordheim, L. Electron emission in intense electric fields. *Proc. R. Soc. Lond. A* **1928**, *119*, 173–181.

Disclaimer/Publisher’s Note: The statements, opinions and data contained in all publications are solely those of the individual author(s) and contributor(s) and not of MDPI and/or the editor(s). MDPI and/or the editor(s) disclaim responsibility for any injury to people or property resulting from any ideas, methods, instructions or products referred to in the content.